

# Drop-Casting Halide Microcrystals Enabled by Green Glycol Solvent for High-Performance Photodetectors

Zhengxun Lai, Fei Wang, You Meng, Xiuming Bu, Dong Chen, Dengji Li, Wei Wang, Chuntai Liu, SenPo Yip, and Johnny C. Ho\*

Halide perovskites have attracted significant recent attention due to their remarkable photoelectric properties; however, the poor structural and moisture stability limit their use for practical utilization. Interestingly, binary halides, such as  $\text{BiI}_3$  and  $\text{PbI}_2$ , are the typical constituents of halide perovskites, where they do not only have the similar outstanding properties of perovskites but also the superior stability. Herein, the synthesis of layered  $\text{BiI}_3$  and  $\text{PbI}_2$  microcrystals by simple drop-casting is investigated and their enhanced photoelectric performance compared to the thin-film counterparts obtained by conventional spin-coating is demonstrated. For the formation of high-quality layered microcrystals, the keys are adopting glycol as a green solvent and appropriate temperature during processing. Once configured into photodetectors, the  $\text{BiI}_3$  and  $\text{PbI}_2$  microcrystals exhibit a higher photocurrent, on/off current ratio, responsivity, and other performance parameters than their thin-film devices. These improved performances of microcrystals can be attributed to their superior crystallinity, thanks to the excellent solvent properties of glycol and the optimal growth temperature chosen. This work proposes a more simple and effective solution processing technique to fabricate layered binary halides with higher quality than the conventional spin-coating method, enabling the further development of halides-based optoelectronic devices.

perovskites-based solar cells, photodetectors, and light emitting diodes have already made fruitful progress in improving their device performance.<sup>[1–5]</sup> However, the stability of halide perovskites in the ambient environment is still fairly poor, which dramatically hinders them from practical utilization.<sup>[6–8]</sup> Besides, it is also challenging to achieve good structural stability for halide perovskites because they have a tight tolerance of appropriate atom size and radius for the intact and stable perovskite structure.<sup>[9,10]</sup> At the same time, the binary halides of  $\text{BiI}_3$  and  $\text{PbI}_2$  are the two major components of halide perovskites,<sup>[11–14]</sup> where their simple structure, particularly without any organic cations, makes them robust with the excellent structural and moisture stability.<sup>[15,16]</sup> Unlike the halide perovskites, there are very few studies focused on these charming binary halides.

$\text{BiI}_3$  is one kind of nontoxic halides, which is also supposed to have high photoelectric performance. The bandgap of  $\text{BiI}_3$  is around 1.67 eV, where it can absorb almost all the visible spectrum and is suitable for applications in solar cells and broadband photodetectors.<sup>[17]</sup> Nevertheless, the quality of  $\text{BiI}_3$  films fabricated by the conventional spin coating method is very poor. Extensive pinholes and gaps are always present in the  $\text{BiI}_3$  films.<sup>[18–20]</sup> Although several techniques, such as thermal annealing, solvent vapor annealing, and antisolvent

## 1. Introduction

In recent years, due to their outstanding electrical and photoelectric properties, halide perovskites have attracted great attention in the scientific community. For example, the halide

tions in solar cells and broadband photodetectors.<sup>[17]</sup> Nevertheless, the quality of  $\text{BiI}_3$  films fabricated by the conventional spin coating method is very poor. Extensive pinholes and gaps are always present in the  $\text{BiI}_3$  films.<sup>[18–20]</sup> Although several techniques, such as thermal annealing, solvent vapor annealing, and antisolvent

Z. Lai, F. Wang, Y. Meng, X. Bu, D. Chen, D. Li, W. Wang, J. C. Ho  
Department of Materials Science and Engineering  
City University of Hong Kong  
Kowloon 999077, Hong Kong SAR  
E-mail: johnnyho@cityu.edu.hk

F. Wang  
State Key Laboratory of Luminescence and Applications  
Changchun Institute of Optics  
Fine Mechanics and Physics, Chinese Academy of Sciences  
Changchun 130021, China

 The ORCID identification number(s) for the author(s) of this article can be found under <https://doi.org/10.1002/adpr.202200041>.

© 2022 The Authors. Advanced Photonics Research published by Wiley-VCH GmbH. This is an open access article under the terms of the Creative Commons Attribution License, which permits use, distribution and reproduction in any medium, provided the original work is properly cited.

DOI: 10.1002/adpr.202200041

Y. Meng, J. C. Ho  
State Key Laboratory of Terahertz and Millimeter Waves  
City University of Hong Kong  
Kowloon 999077, Hong Kong SAR

C. Liu  
Key Laboratory of Advanced Materials Processing & Mold (Zhengzhou University)  
Ministry of Education  
Zhengzhou 450002, China

S. P. Yip, J. C. Ho  
Institute for Materials Chemistry and Engineering  
Kyushu University  
Fukuoka 816-8580, Japan

treatment, have been applied in combination with spin-coating, the crystal quality and optoelectronic performance of the obtained films are still not satisfactory.<sup>[21,22]</sup> For instance, Chang et al. have fabricated high-quality BiI<sub>3</sub> films by thermal evaporation, but a graphene seed layer is necessary for this method.<sup>[23]</sup> Qu and his team incorporated CuI into the precursor solution of BiI<sub>3</sub>, but large pinholes still existed during the film formation, together with the insufficient photodetector performance.<sup>[24]</sup> This way, it is highly desirable to develop simple techniques to achieve high-quality BiI<sub>3</sub> films for enhanced device performance.

PbI<sub>2</sub> is another halide semiconductor mainly used as a precursor for the synthesis of lead halides-based perovskite materials.<sup>[14,16,25–27]</sup> It is interesting that the PbI<sub>2</sub> itself is also a promising photoelectric material. More importantly, it is well known that PbI<sub>2</sub> is a decomposition product of many lead halide perovskites (e.g., methylammonium lead iodide) when they degrade in ambient environments. Therefore, PbI<sub>2</sub> is much more stable than the perovskites. Nonetheless, there are still limited reports of PbI<sub>2</sub> and its applications in optoelectronic devices.

Herein, we develop a simple drop-casting method to fabricate high-quality layered BiI<sub>3</sub> and PbI<sub>2</sub> microcrystals (MCs), in which this technique can be easily applied in industrial production. In specific, the green solvent of glycol is identified as the most appropriate solvent for drop-casting here. After controllably dripping the precursor solution onto the substrate and heating it for rapid evaporation of the solvent, high-quality BiI<sub>3</sub> and PbI<sub>2</sub> MCs are obtained. When these MCs are configured into simple photodetectors, their device performance is impressive and superior to the thin film counterparts fabricated by conventional spin-coating. The glycol solvent and the growth temperature chosen are responsible for the high-quality MCs, which are also demonstrated and discussed. All these results can provide valuable material design and processing guidelines to break down the barriers that hinder the development of halides-based optoelectronic devices as well as to fill the technology gap of high-performance BiI<sub>3</sub>- and PbI<sub>2</sub>-based photodetectors.

## 2. Results and Discussion

In this work, the drop-casting method is employed to fabricate layered BiI<sub>3</sub> and PbI<sub>2</sub> MCs as depicted in **Figure 1a**, together with

their crystal structures described in **Figure 1b,c**. In principle, both have layered structures, where Bi or Pb atoms are coordinated with six I atoms. For BiI<sub>3</sub>, every I atom bonds to two Bi atoms, while for PbI<sub>2</sub>, each I atom bonds to three Pb atoms. To prepare the MCs, the glass substrates are first ultrasonically cleaned with acetone, ethanol, and deionized (DI) water, followed by the oxygen plasma treatment to improve their hydrophilia. 5  $\mu$ L of BiI<sub>3</sub> or PbI<sub>2</sub> solution, with glycol as the solvent, is then controllably dripped onto the substrates. Next, the processed substrates are thermally heated on hot plates for 5 min with temperatures of 60 and 80 °C for the formation of BiI<sub>3</sub> and PbI<sub>2</sub> MCs, respectively. It is worth mentioning that in the conventional spin coating method, most of the precursor solution is wasted and not consumed for the film formation during the process. Fortunately, this drop-casting technique omits the procedure of spin coating, which can not only improve the quality of the products and simplify the preparation process but also save the precursor solution, being beneficial to large-scale production.

After the formation of BiI<sub>3</sub> MCs, it is crucial to investigate their structural quality and crystallinity. The X-Ray diffraction (XRD) pattern of the MCs is first collected and compiled in **Figure 2a**, where the peaks can be perfectly indexed to the standard XRD pattern (PDF#89-0307), suggesting that the pure phase BiI<sub>3</sub> is obtained. The UV–vis absorption spectrum of the BiI<sub>3</sub> MCs is also shown in **Figure 2b**. It is observed that the absorption edge is located at 695 nm, indicating the microcrystals being capable of absorbing most of the visible light for highly efficient photovoltaic applications.<sup>[22,28]</sup> **Figure 2c** and S1, Supporting Information, demonstrate the high-resolution and large-area scanning electron microscope (SEM) image of the BiI<sub>3</sub> MCs. One can see that the MCs have a regular hexagonal shape with edge lengths of  $\approx 50 \mu\text{m}$ , which is consistent with the hexagonal symmetry of BiI<sub>3</sub> in the space group of R $\bar{3}$ .<sup>[29,30]</sup> Combined with the XRD results, it is revealed that most of the MCs are oriented horizontally, having an out-of-plane direction of [300], which is also consistent with the stacking direction of BiI<sub>3</sub> layers. The existence of the XRD peak of (11-3) is attributed to the hexagonal plates standing vertically rather than lying flat on the substrate (**Figure S1**, Supporting Information). Based on the large-area AFM image (**Figure 2d**,

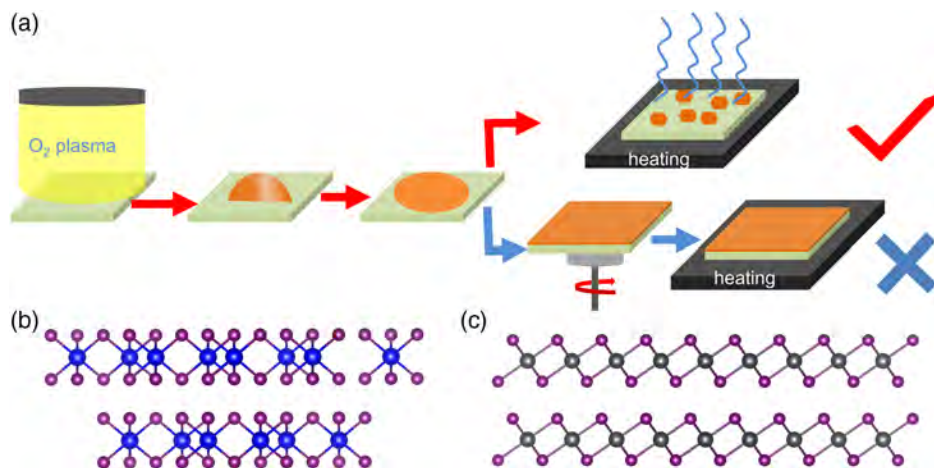


**Figure 1.** a) Schematic illustration of the drop-casting method and conventional spin coating method. Crystal structure of: b) BiI<sub>3</sub> and c) PbI<sub>2</sub>.

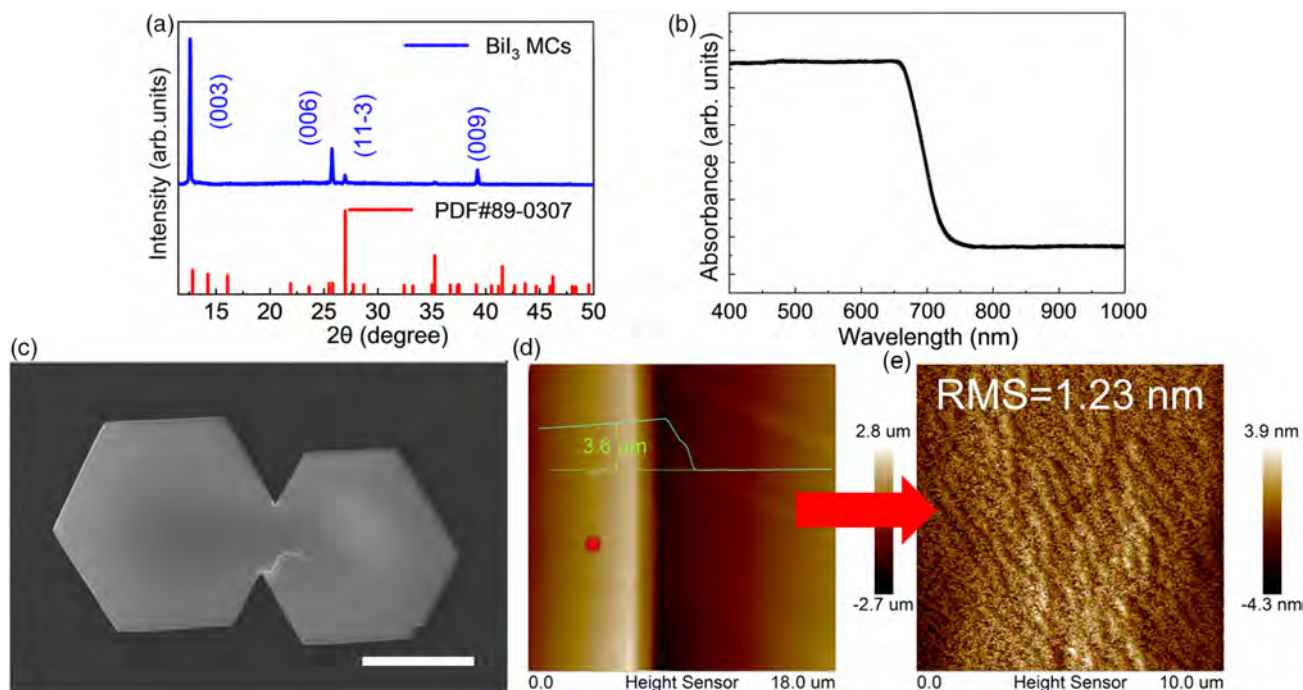


**Figure 2.** a) X-ray diffraction (XRD) pattern; b) Absorption spectrum; c) Scanning electron microscope (SEM) image (the scale bar is 50  $\mu\text{m}$ ); d) Large area atomic force microscope (AFM) image; e) High-resolution AFM image of the  $\text{PbI}_2$  microcrystals (MCs).

Supporting Information), the typical thickness of the  $\text{BiI}_3$  MCs is determined to be 3.6  $\mu\text{m}$ . The surface of the MCs is found to be very smooth with a root mean square (RMS) roughness as low as 1.23 nm (Figure 2e, Supporting Information). For comparison, the  $\text{BiI}_3$  film is also fabricated by the conventional spin-coating method with the corresponding XRD pattern collected (Figure S2, Supporting Information). All the peaks are fitted well to the data from PDF #89-0307, which designates the formation of the pure phase  $\text{BiI}_3$ . The absorption spectrum of the film suggests that it has a bandgap of 1.64 eV (Figure S3, Supporting Information). The thickness of the film is as well determined to be about 480 nm by the AFM image in Figure S4, Supporting Information. However, the obtained SEM image displays many obvious pinholes that existed on the film surface (Figure S5, Supporting Information). The AFM image in Figure S6, Supporting Information, also indicates that its RMS roughness is as large as 138 nm. This poor quality of the  $\text{BiI}_3$  film fabricated by spin-coating has been widely reported in the literature.<sup>[20,24,28,31]</sup> All these results clearly show the successful construction of the  $\text{BiI}_3$  MCs with good crystal quality and surface smoothness readily achieved by simple drop-casting.

After that, the  $\text{BiI}_3$  MCs and spin-coated films are configured into simple photodetectors to evaluate and compare their photoelectric device performance. The schematic diagram of the detector structure is depicted in the inset of Figure 3b. The current–voltage ( $I$ – $V$ ) curves of the MCs under different light intensities are shown in Figure S7, Supporting Information, where a 532 nm laser is used as the illumination source. All the  $I$ – $V$  curves exhibit a linear relationship, suggesting the nearly ohmic contact properties, which can contribute to the effective collection of photogenerated carriers. The on/off current ratio

of the MCs-based photodetector is determined to be  $2.2 \times 10^4$ . Figure 3a shows the current–time ( $I$ – $t$ ) curves of the MCs and thin-film photodetectors under chopped illumination with an intensity of  $750 \text{ mW cm}^{-2}$ . It is clear that the on/off switching characteristics of both photodetectors are very stable. By considering the adoption of the same device geometry, the photocurrent of the MCs device is about five times larger than that of the thin-film device. The photocurrents under different light intensities are also depicted in Figure 3b. The photocurrents of both MCs and thin-film devices show a sublinear relationship with the light intensities, which is usually due to the complex processes of electron-hole generation, trapping, and recombination in the device channels.<sup>[32]</sup> At the same time, linear dynamic range (LDR) is an important performance parameter, representing the linear light intensity response range for a photodetector. LDR can be calculated by the equation of  $\text{LDR} = 20 \log \frac{P_{\text{upper}}}{P_{\text{lower}}}$  where  $P_{\text{upper}}$  and  $P_{\text{lower}}$  are the maximum and minimum light intensity limit within the linearity, respectively. The LDR values of both  $\text{BiI}_3$  MCs and thin-film photodetectors are then calculated to be as large as 77.5 dB. Since the  $P_{\text{upper}}$  and  $P_{\text{lower}}$  values are limited to the laser we use, and the photocurrents still show a consistent response in this working range, the actual LDR value must be larger than this calculated value. Besides, responsivity ( $R$ ) is another crucial performance parameter. It can be calculated according to the equation of  $R = \frac{I_p}{\Phi S}$ , where  $I_p$  is the photocurrent,  $\Phi$  is the light intensity, and  $S$  is the active area of the photodetector.<sup>[33]</sup> As depicted in Figure 3c, it is evident that the largest  $R$  value of the  $\text{BiI}_3$  MCs is  $610 \text{ mA W}^{-1}$  at an intensity of  $0.1 \text{ mW cm}^{-2}$  which is 13.5 times larger than that of the thin-film counterpart ( $45 \text{ mA W}^{-1}$ ). Moreover, detectivity ( $D^*$ )

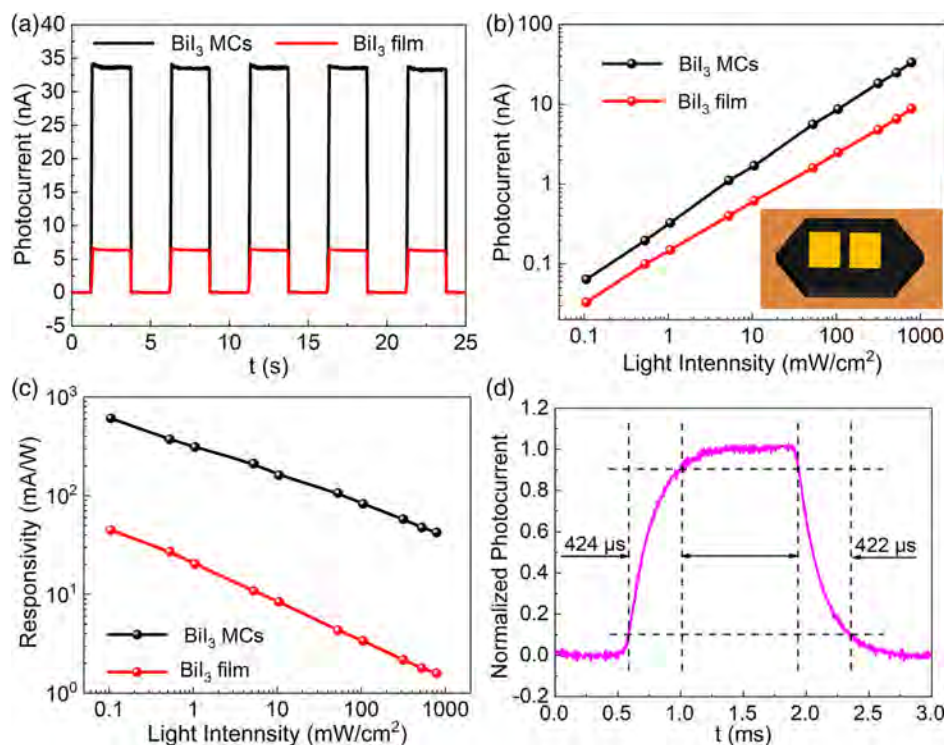


**Figure 3.** a) Time-dependent photoresponse; b) Dependence of photocurrent on light intensity and the inset shows the schematic of the device structure; c) Dependence of responsivity on the light intensity of the BiI<sub>3</sub> MCs and film; d) High-resolution current versus time curve for the BiI<sub>3</sub> MCs.

and external quantum efficiency (EQE) are other important performance matrices of photodetectors, which can be defined as  $D^* = RS^{1/2}/(2eI_{\text{dark}})^{1/2}$  and  $\text{EQE} = hcR/e\lambda$ .<sup>[34]</sup> The parameters of  $e$ ,  $I_{\text{dark}}$ ,  $h$ ,  $c$ , and  $\lambda$  represent the electronic charge, dark current, Planck's constant, velocity of the incident light, and wavelength of the incident light, respectively. As presented in Figure S8, Supporting Information, the  $D^*$  and EQE values of the photodetectors are calculated. It is not surprising that the  $D^*$  and EQE values of the BiI<sub>3</sub> MCs are found to be much larger than those of the film, where the largest  $D^*$  and EQE arrive at  $8.8 \times 10^{11}$  Jones and 142% at an intensity of  $0.1 \text{ mW cm}^{-2}$ , respectively. Based on the high-resolution  $I-t$  curve, the response speeds of the photodetectors can be determined, where these transient behaviors are essential for high-frequency devices. The rise time is typically defined as the time required for current to increase from 10% to 90% of its peak value, and similarly, the decay time is from 90% to 10% of the peak value. In this work, the rise and decay times of the BiI<sub>3</sub> MCs photodetector is extracted to be 424 and 422  $\mu\text{s}$ , accordingly (Figure 3d), which are much faster than those of the thin-film device (Figure S9, Supporting Information). These better responsivity, detectivity, EQE, and response speeds of the BiI<sub>3</sub> MCs can be attributed to the superior crystallinity of the spin-coated film.

Apart from BiI<sub>3</sub> MCs, this drop-casted technique can also be applied to the synthesis of other binary halide MCs, such as PbI<sub>2</sub>. As shown in the XRD pattern in Figure 4a, there are only the peaks of the lattice planes along [005] direction witnessed, which is also the stacking direction of the PbI<sub>2</sub> layers. This XRD result agrees perfectly with the SEM images presented in Figure 4c and

S10, Supporting Information, that all the PbI<sub>2</sub> MCs are horizontally oriented on the substrate surface, which is a distinct contrast to the BiI<sub>3</sub> MCs with a portion of MCs standing vertically. In this case, this out-of-plane direction demonstrates the crystal planes of the hexagonal PbI<sub>2</sub> crystals, where the edge lengths of the MCs are  $\approx 20 \mu\text{m}$ .<sup>[35]</sup> The UV-vis absorption spectrum of the PbI<sub>2</sub> MCs is also shown in Figure 4b. The absorption edge is found to be located at 508 nm, suggesting a bandgap of 2.44 eV. Figure 4d demonstrates the AFM image of one typical PbI<sub>2</sub> MC, in which the thickness is determined to be around 170 nm. The corresponding high-resolution AFM image is also measured and displayed in Figure 4e, revealing the very smooth surface morphology with the RMS roughness of only 0.38 nm. For comparison, the XRD pattern and SEM image of the PbI<sub>2</sub> film fabricated by spin-coating are also shown in Figure S11 and S12, Supporting Information. There are only the obvious peaks of the lattice planes along the [005] direction in the XRD pattern, suggesting the pure phase PbI<sub>2</sub> film with high crystallinity, which can be confirmed by the distinct grains without any significant cracks or pinholes observed in the SEM image. The thickness of about 1  $\mu\text{m}$  and RMS roughness of 35 nm of the film can also be acquired from the AFM images in Figure S13 and S14, Supporting Information. The absorption spectrum of the PbI<sub>2</sub> film indicates its bandgap of 2.44 eV (Figure S15, Supporting Information). All these findings designate the good crystallinity of our drop-casted PbI<sub>2</sub> MCs.

The photoelectric performance of the PbI<sub>2</sub> MCs and thin-film photodetectors is also thoroughly characterized. The  $I-V$  curves of the MCs under different light intensities are shown in

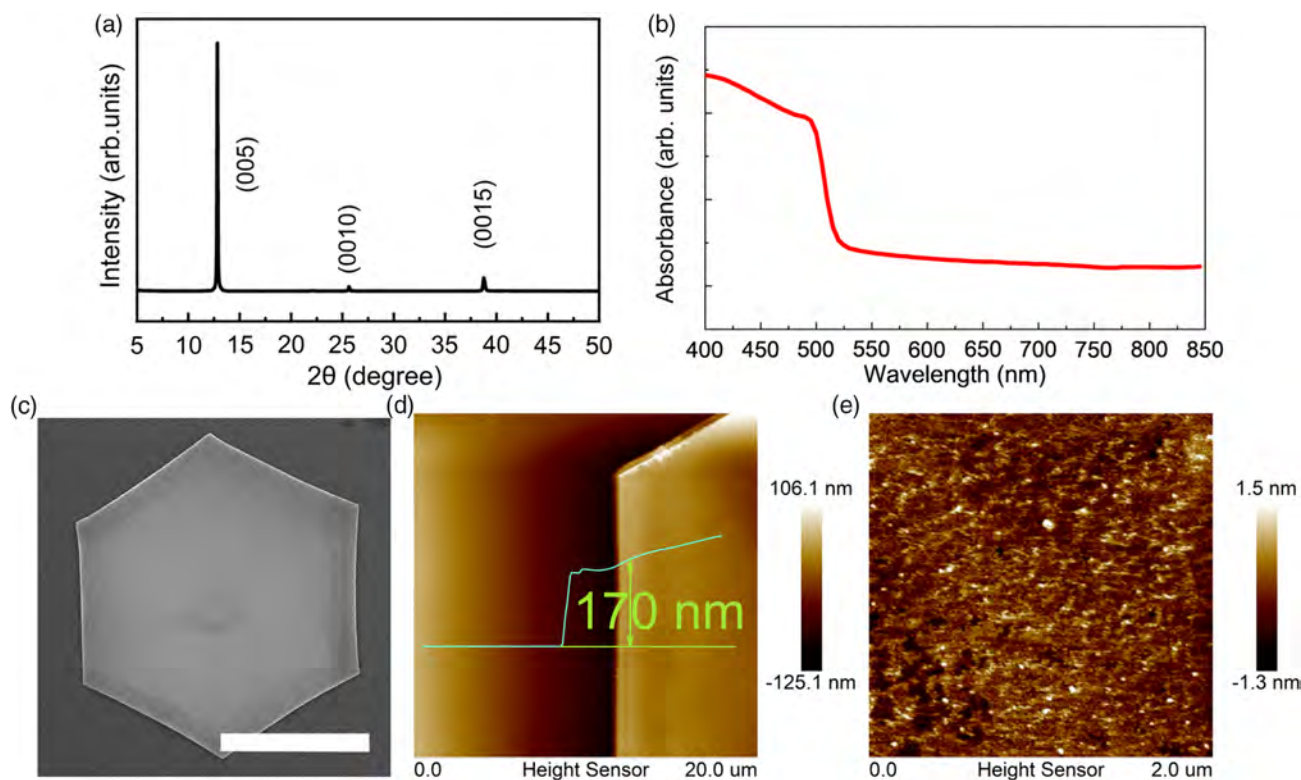


**Figure 4.** a) XRD pattern; b) Absorption spectrum; c) SEM image (the scale bar is 20  $\mu\text{m}$ ); d) Large area AFM image; e) High-resolution AFM image of the  $\text{PbI}_2$  MCs.

Figure S16, Supporting Information, where a 450 nm laser is used for the measurement. All the  $I$ - $V$  curves exhibit a linear relationship, indicating the nearly ohmic contact properties between metal electrodes and device channels. This efficient contact is beneficial for the effective collection of photogenerated carriers. The on/off current ratio of the MCs photodetector is determined to be as large as  $2.9 \times 10^5$ . As shown in the  $I$ - $t$  curves in **Figure 5a**, both MCs and thin-film photodetectors give repeatable on/off switching characteristics under chopped illumination with an intensity of  $730 \text{ mW cm}^{-2}$ . The photocurrent of the MCs is more than five times larger than that of the thin-film counterpart with the same device geometry. Similar to the case of  $\text{BiI}_3$ , the photocurrents of both  $\text{PbI}_2$  MCs and thin-film devices display a sub-linear relationship with the light intensities (**Figure 5b**), which is mainly attributed to the generation, trapping, and recombination of photocarriers in the device channel. The LDR values of both photodetectors are calculated to be around 81 dB. Just as demonstrated earlier, the actual LDR values are anticipated to be larger than this value of 81 dB. In contrast, the  $R$  values of the photodetectors are calculated and presented in **Figure 5c**. It is witnessed that the responsivity of the  $\text{PbI}_2$  MCs device is more than three times larger than that of the thin-film device, where the largest  $R$  is determined to be  $17 \text{ mA W}^{-1}$  at an intensity of  $0.1 \text{ mW cm}^{-2}$ . This superior responsivity of the  $\text{PbI}_2$  MCs is mostly resulted from the higher crystallinity than the thin film. The  $D^*$  and EQE values of the photodetectors are as well depicted in **Figure S17**, Supporting Information. Similar to the responsivity, the  $D^*$  and EQE of the  $\text{PbI}_2$  MCs are much

larger than those of the film, accordingly. One can see that although the EQE of the  $\text{PbI}_2$  MCs is not very high (about 4.6%) due to the intrinsic nature of  $\text{PbI}_2$ , the  $D^*$  is as high as  $1.4 \times 10^{11}$  Jones because of the high on/off ratio. In addition, the response speed of the  $\text{PbI}_2$  MCs photodetector can be determined through the high-resolution  $I$ - $t$  curve. The rise and decay times are found to be as short as 154 and 153  $\mu\text{s}$ , respectively (**Figure 5d**), being superior to those of thin-film counterparts (**Figure S18**, Supporting Information). **Table 1** summarizes the reported figure of merits of halides-based photodetectors. It is remarkable that the performance of the photodetectors fabricated by simple drop-casting developed in this work is highly comparable or even better performed than others reported recently, including the nanostructures fabricated by chemical (physical) vapor deposition methods.<sup>[16,29,36]</sup>

Furthermore, it is worth mentioning that the solvent and the heating temperature are crucial factors to obtain high-quality MCs. For the formation of high-quality crystals, a proper growth temperature and a slow evaporation rate are necessary. To control the evaporation rate, the properties of the solvent used in this method are crucial factors that needed to be considered. Generally, high boiling point and viscosity, and low vapor pressure can reduce the evaporation rate of the solvent. Accordingly, several solvents that can effectively dissolve  $\text{BiI}_3$  and  $\text{PbI}_2$  are explored and compiled in **Table S1**, Supporting Information. As compared with other solvents, glycol has a much higher boiling point and viscosity and a much lower vapor pressure. This way, glycol is the overwhelming choice for this drop-casting

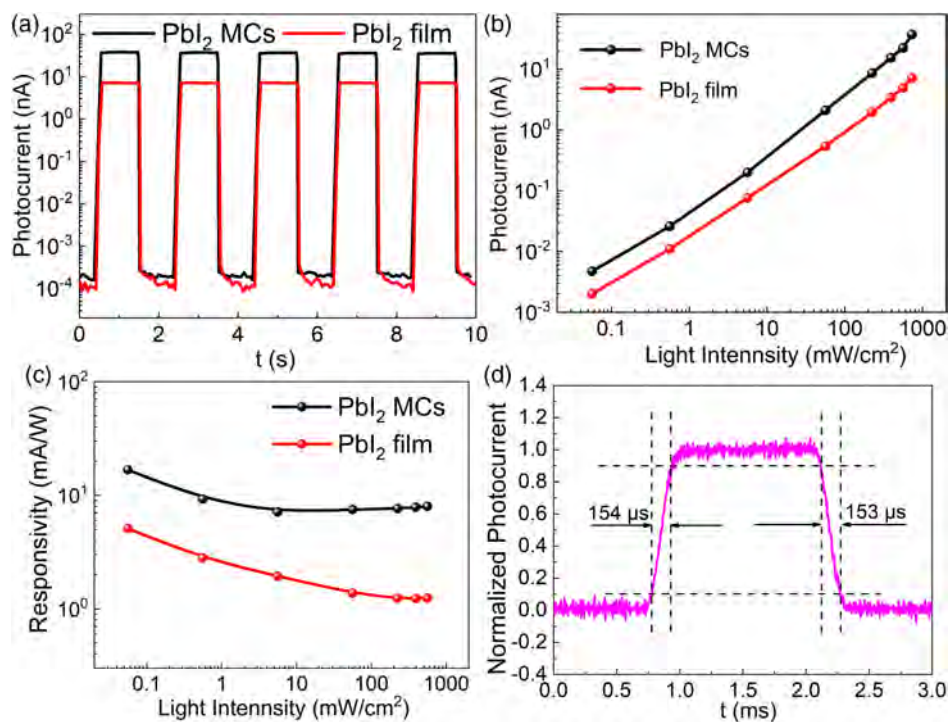


**Figure 5.** a) Time-dependent photoresponse; b) Dependence of photocurrent on light intensity; c) Dependence of responsivity on the light intensity of the PbI<sub>2</sub> MCs and film; d) High-resolution current versus time curve for the PbI<sub>2</sub> MCs.

**Table 1.** Comparison of various figures of merits of halides-based photodetectors.

Halides	Bias [V]	Light	$R$ [mA W <sup>-1</sup> ]	$D^*$ [Jones]	Rise/decay time [ms]	References
PbI <sub>2</sub>	5	450 nm	410	$3.1 \times 10^{11}$	86/150	[16]
BiI <sub>3</sub>	3	532 nm	$5.3 \times 10^{-5}$	$4.0 \times 10^4$	N/A	[24]
CuBiI <sub>4</sub>	3	532 nm	500	$3.8 \times 10^7$	Several thousands	[24]
BiI <sub>3</sub>	5	635 nm	2220	$1.65 \times 10^{12}$	2/5.3	[29]
BiI <sub>3</sub>	5	635 nm	2800	$1.2 \times 10^{12}$	3/9	[36]
PbI <sub>2</sub>	1.9	450 nm	0.1	N/A	0.055/0.11	[37]
SbSI	0.1	White light	0.01	$10^9$	8/33	[38]
SbI <sub>3</sub>	6	450 nm	1.11	$1.8 \times 10^9$	196.1/205.7	[39]
BiI <sub>3</sub>	1.5	532 nm	608	$8.8 \times 10^{11}$	0.424/0.422	This work
PbI <sub>2</sub>	1.5	450 nm	17	$1.4 \times 10^{11}$	0.154/0.153	

method. The SEM images of the PbI<sub>2</sub> fabricated by drop-casting with dimethylformamide (DMF) and water as solvents are also shown in Figure S19, Supporting Information. It is obvious that the PbI<sub>2</sub> films are obtained when DMF is used as the solvent. However, the products made with the solution using water as solvent show some irregular clusters. The undesired products must be caused by the fast evaporation rate of DMF and water, which makes the formation of too high a concentration of nucleus and then decreases the sizes and quality of the crystals. In addition, as mentioned earlier, the growth temperature can

also directly influence the crystal quality. Figure S20, Supporting Information, demonstrates the SEM images of the MCs fabricated with the solution using glycol as the solvent, where the heating temperature is changed from 40 to 140 °C. When the temperature is relatively low between 40 and 60 °C, the MCs do not appear in regular hexagons. As the temperature increases later from 100 to 140 °C, the MCs would adhere to each other gradually. It is because when the temperature is high, the higher evaporation rate of the solvent will make the crystal nucleate immediately at numerous nucleation sites; in this case, the films of microcrystals become denser. As a result, the solvent with high boiling point and viscosity and low vapor pressure, as well as appropriate heating temperature, are necessary to fabricate high-quality MCs by drop-casting.

### 3. Conclusion

In conclusion, layered BiI<sub>3</sub> and PbI<sub>2</sub> MCs have been directly fabricated by drop-casting and later configured into photodetectors. Their thin-film counterparts have also been fabricated by conventional spin coating, followed by a detailed comparison among their crystallinity and photoelectric device properties. The MCs photodetectors are found to show a much higher performance than that of the films. Specifically, the responsivity of the BiI<sub>3</sub> MCs device can reach 608 mA W<sup>-1</sup>, which is more than 13 times larger than that of the thin-film device. Besides, the on/off ratio of the PbI<sub>2</sub> MCs photodetector is determined to be as large as  $2.9 \times 10^5$ , where the responsivity is also five times larger than that of the thin-film counterpart. These superior performances

of the layered MCs can be attributed to their high crystallinity brought about by drop-casting. The high-quality MCs are confirmed to be ascribed to the glycol solvent and optimal growth temperature, where the mechanism is detailly demonstrated and studied. All these results would deliver valuable insights to fabricate high-quality layered halide MCs and break the bottleneck of the poor performance of binary halide thin-film devices.

## 4. Experimental Section

**Synthesis of Materials:** For the solution used in drop-casting, 0.3 M BiI<sub>3</sub> and 0.1 M PbI<sub>2</sub> were dissolved in glycol and then filtered through a 0.2 μm polytetrafluoroethylene filter. For the solution used in spin-coating, 1 M BiI<sub>3</sub> and 0.5 M PbI<sub>2</sub> were dissolved in DMF and also filtered through a 0.2 μm polytetrafluoroethylene filter to obtain a clear solution.

**Device Fabrication:** The glass substrates were first ultrasonically washed with acetone, ethanol, and deionized (DI) water for 15 min in succession. Then, these substrates were treated with mild oxygen plasma to improve their hydrophilia. For the drop-casting method, 4 μL of BiI<sub>3</sub> or PbI<sub>2</sub> solution dissolved in glycol was dripped on the substrate, followed by thermal annealing at 60 or 80 °C for 5 min. For the spin-coating method, 30 μL of BiI<sub>3</sub> or PbI<sub>2</sub> solution dissolved in DMF was spin-coated on the substrate at 3000 rpm for 30 s, followed by thermal annealing at 100 or 250 °C for 10 min. For the configuration of the photodetectors, 50 nm thick Au electrodes were thermally evaporated onto the samples with the assistance of a shadow mask, where the channel length and width are 10 and 70 μm, respectively.

**Film and Device Characterization:** XRD (D2 Phaser with Cu Kα radiation, Bruker) was used to evaluate the crystal structure of the obtained MCs and thin films. The morphologies of the MCs and thin films were characterized by SEM (FEI Quanta 450 FEG SEM). The thickness and the surface roughness of the MCs were characterized by AFM (Bruker Dimension Icon AFM). UV–vis absorption spectra were recorded using a Hitachi UH4150 UV–vis NIR Spectrophotometer. The electrical performance of fabricated devices was characterized by a standard electrical probe station and an Agilent 4155C semiconductor analyzer (Agilent Technologies, California, USA). Lasers with wavelength of 532 and 450 nm were used as the light sources for the photodetector measurement, while the power of the incident irradiation was measured using a power meter (PM400, Thorlabs). An attenuator was also employed to tune the irradiation power illuminating the device. For determining the response time of the detector, a low-noise current amplifier (SR570, Stanford Research Systems, USA) combined with a digital oscillator (TBS 1102B EDU, Tektronix, USA) was used to obtain high-resolution current–time curves.

## Supporting Information

Supporting Information is available from the Wiley Online Library or from the author.

## Acknowledgements

The authors acknowledge the General Research Fund (CityU 11306520) and the Theme-based Research (T42-103/16-N) of the Research Grants Council of Hong Kong SAR, China, and the Foshan Innovative and Entrepreneurial Research Team Program (No. 2018IT100031).

## Conflict of Interest

The authors declare no conflict of interest.

## Data Availability Statement

The data that support the findings of this study are available from the corresponding author upon reasonable request.

## Keywords

BiI<sub>3</sub>, drop-casting, halide microcrystals, PbI<sub>2</sub>, photodetectors

Received: February 23, 2022

Revised: May 9, 2022

Published online: May 29, 2022

- [1] Y. Zhao, K. Zhu, *Chem. Soc. Rev.* **2016**, *45*, 655.
- [2] A. K. Jena, A. Kulkarni, T. Miyasaka, *Chem. Rev.* **2019**, *119*, 3036.
- [3] H. P. Wang, S. Li, X. Liu, Z. Shi, X. Fang, J. H. He, *Adv. Mater.* **2020**, *33*, 2003309.
- [4] L. Cao, X. Liu, Y. Li, X. Li, L. Du, S. Chen, S. Zhao, C. Wang, *Front. Phys.* **2021**, *16*, 33201.
- [5] L. Lei, Q. Dong, K. Gundogdu, F. So, *Adv. Funct. Mater.* **2021**, *31*, 2010144.
- [6] N. Ali, S. Rauf, W. Kong, S. Ali, X. Wang, A. Khesro, C. P. Yang, B. Zhu, H. Wu, *Renewable Sustainable Energy Rev.* **2019**, *109*, 160.
- [7] F. Arabpour Roghabadi, M. Alidaei, S. M. Mousavi, T. Ashjari, A. S. Tehrani, V. Ahmadi, S. M. Sadrameli, *J. Mater. Chem. A* **2019**, *7*, 5898.
- [8] Q. Fan, G. V. Biesold-mcgee, J. Ma, Q. Xu, S. Pan, J. Peng, Z. Lin, *Angew. Chem., Int. Ed.* **2020**, *59*, 1030.
- [9] M. Liu, N. Jiang, H. Huang, J. Lin, F. Huang, *Chem. Eng. J.* **2020**, *413*, 127547.
- [10] W. C. Qiao, J. Yang, W. Dong, G. Yang, Q. Bao, R. Huang, X. L. Wang, Y. F. Yao, *NPG Asia Mater.* **2020**, *12*, 68.
- [11] H. E. Ali, Y. Khairy, *Vacuum* **2020**, *180*, 109640.
- [12] R. A. Ismail, A. M. Mousa, S. S. Shaker, *Optik* **2020**, *202*, 163585.
- [13] R. A. Ismail, A. M. Mousa, M. H. Amin, *Mater. Res. Express* **2018**, *5*, 115024.
- [14] C. Ran, W. Gao, N. Li, Y. Xia, Q. Li, Z. Wu, H. Zhou, Y. Chen, M. Wang, W. Huang, *ACS Energy Lett.* **2019**, *4*, 358.
- [15] H. Zheng, W. Wang, S. Yang, Y. Liu, J. Sun, *RSC Adv.* **2016**, *6*, 1611.
- [16] C. Lan, R. Dong, Z. Zhou, L. Shu, D. Li, S. P. Yip, J. C. Ho, *Adv. Mater.* **2017**, *29*, 1702759.
- [17] N. J. Podraza, W. Qiu, B. B. Hinojosa, H. Xu, M. A. Motyka, S. R. Phillpot, J. E. Baciak, S. Trolier-Mckinstry, J. C. Nino, *J. Appl. Phys.* **2013**, *114*, 033110.
- [18] U. H. Hamdeh, R. D. Nelson, B. J. Ryan, U. Bhattacharjee, J. W. Petrich, M. G. Panthani, *Chem. Mater.* **2016**, *28*, 6567.
- [19] S. Ma, Y. Yang, C. Liu, M. Cai, Y. Ding, Z. Tan, P. Shi, S. Dai, A. Alsaedi, T. Hayat, *ACS Appl. Mater. Interfaces* **2019**, *11*, 32509.
- [20] U. H. Hamdeh, R. D. Nelson, B. J. Ryan, M. G. Panthani, *J. Phys. Chem. C* **2019**, *123*, 13394.
- [21] A. Kulkarni, T. Singh, A. K. Jena, P. Pinpathak, M. Ikegami, T. Miyasaka, *ACS Appl. Mater. Interfaces* **2018**, *10*, 9547.
- [22] J. Kang, S. Chen, X. Zhao, H. Yin, W. Zhang, M. Al-Mamun, P. Liu, Y. Wang, H. Zhao, *Nano Energy* **2020**, *73*, 104799.
- [23] P. H. Chang, C. S. Li, F. Y. Fu, K. Y. Huang, A. S. Chou, C. I. Wu, *Adv. Funct. Mater.* **2018**, *28*, 1800179.
- [24] N. Qu, Y. Lei, X. Yang, X. Hu, W. Zhao, C. Zhao, Z. Zheng, *J. Mater. Chem. C* **2020**, *8*, 8451.

- [25] R. A. Ismail, A. M. Mousa, K. S. Khashan, M. H. Mohsin, M. K. Hamid, *J. Mater. Sci. Mater. Electron.* **2016**, *27*, 10696.
- [26] Q. Liang, J. Han, H. Li, L. Chen, Z. Xie, J. Liu, Y. Han, *Org. Electron.* **2018**, *53*, 26.
- [27] J. Wang, D. Lin, T. Zhang, M. Long, T. Shi, K. Chen, Z. Liang, J. Xu, W. Xie, P. Liu, *CrystEngComm* **2019**, *21*, 736.
- [28] Y. Wang, X. Shi, G. Wang, J. Tong, D. Pan, *J. Mater. Chem. C* **2020**, *8*, 14066.
- [29] Q. Wei, Y. Wang, J. Yin, Y. Xia, Z. Liu, *Adv. Electron. Mater.* **2019**, *5*, 1900159.
- [30] Y. Zhu, Q. Zhang, M. Kam, S. Poddar, L. Gu, S. Liang, P. Qi, F. Miao, Z. Fan, *InfoMat* **2020**, *2*, 975.
- [31] D. Tiwari, D. Alibhai, D. J. Fermin, *ACS Energy Lett.* **2018**, *3*, 1882.
- [32] F. Binet, J. Y. Duboz, E. Rosencher, F. Scholz, V. Härle, *Appl. Phys. Lett.* **1996**, *69*, 1202.
- [33] Z. Lai, R. Dong, Q. Zhu, Y. Meng, F. Wang, F. Li, X. Bu, X. Kang, H. Zhang, Q. Quan, W. Wang, F. Wang, S. Yip, J. C. Ho, *ACS Appl. Mater. Interfaces* **2020**, *12*, 39567.
- [34] Y. Meng, C. Lan, F. Li, S. Yip, R. Wei, X. Kang, X. Bu, R. Dong, H. Zhang, J. C. Ho, *ACS Nano* **2019**, *13*, 6060.
- [35] X. Yang, D. Luo, Y. Xiang, L. Zhao, M. Anaya, Y. Shen, J. Wu, W. Yang, Y. Chiang, Y. Tu, R. Su, Q. Hu, H. Yu, G. Shao, W. Huang, T. P. Russell, Q. Gong, S. D. Stranks, *Adv. Mater.* **2021**, *33*, 2006435.
- [36] Q. Wei, J. Chen, P. Ding, B. Shen, J. Yin, F. Xu, Y. Xia, Z. Liu, *ACS Appl. Mater. Interfaces* **2018**, *10*, 21527.
- [37] W. Zheng, Z. Zhang, R. Lin, K. Xu, J. He, F. Huang, *Adv. Electron. Mater.* **2016**, *2*, 1600291.
- [38] K. C. Gödel, U. Steiner, *Nanoscale* **2016**, *8*, 15920.
- [39] M. Xiao, H. Yang, W. Shen, C. Hu, K. Zhao, Q. Gao, L. Pan, L. Liu, C. Wang, G. Shen, H. X. Deng, H. Wen, Z. Wei, *Small* **2020**, *16*, 1907172.